Philosophical Magazine,
Vol. 86, No. 16, 1 June 2006, 2295–2313

Taylor & Francis
Taylor & Francis Group

Atomic-scale study of dislocation–stacking fault tetrahedron interactions. Part I: mechanisms

Y. N. OSETSKY*†, D. RODNEY‡ and D. J. BACON§

†Computer Science and Mathematics Division, Oak Ridge National Laboratory, P. O. Box 2008, Oak Ridge, TN 37831-6138, USA
‡Génie Physique et Mécanique des Matériaux (UMR CNRS 5010), 101 rue de la Physique, BP 46 38402, Saint Martin d'Hères, France
§Materials Science and Engineering, Department of Engineering, University of Liverpool, Brownlow Hill, Liverpool L36 9GH, UK

(*Received 26 August 2005; in final form 7 December 2005*)

Stacking fault tetrahedra (SFTs) are formed under irradiation in fcc metals and alloys. The high number density of SFTs observed suggests that they should contribute to radiation-induced hardening and, therefore, be taken into account when estimating mechanical property changes of irradiated materials. The key issue in this is to describe the interaction between a moving dislocation and an individual SFT, which is distinguished by a small physical size of the order of ~1–10 nm. We have performed atomistic simulations of edge and screw dislocations interacting with SFTs of different sizes at different temperatures and strain rates. Five possible interaction outcomes have been identified, involving either partial absorption, or shearing or restoration of SFTs. The mechanisms that give rise to these processes are described and their dependence on interaction parameters, such as SFT size, dislocation–SFT geometry, temperature and stress/strain rate are determined. Mechanisms that help to explain the formation of defect-free channels cleared by gliding dislocations, as observed experimentally, are also discussed. Hardening due to the various mechanisms and their dependence on loading conditions will be presented in a following paper (Part II).

1. Introduction

Stacking fault tetrahedra (SFTs) are common defects formed in fcc metals by treatments such as irradiation [1–5], ageing after quenching [6–9] and deformation [10–12]. The size and density of the SFTs depend on the treatment: SFTs formed under irradiation conditions, which are of particular interest here, are small and their number density is high compared to other conditions. For example, Singh *et al*. [3] observed SFTs with a mean size of 2.5 ± 0.5 nm and an average separation of 20 nm in Cu irradiated by neutrons for dose levels up to 0.3 dpa at 360 K. Similar results were obtained in nickel irradiated by 590 MeV protons [4]. Such a high density of defects can make a significant change to the mechanical properties of the materials by preventing dislocation motion. Indeed, interaction between moving dislocations

*Corresponding author. Email: osetskiyyn@ornl.gov

Philosophical Magazine
ISSN 1478–6435 print/ISSN 1478–6443 online © 2006 Taylor & Francis
http://www.tandf.co.uk/journals
DOI: 10.1080/14786430500513783

and a population of SFTs has been argued to be the cause of such mechanical effects as strengthening, hardening and plastic instability during deformation. The latter effect is due to a localization of the deformation in shear bands, which are called *clear bands* (or *defect-free channels*), because after deformation they are clear of all irradiation defects visible by transmission electron microscopy (TEM) [3, 13–15]. These processes, which affect the service life-time of structural materials, require investigation by a variety of techniques. In principle, the problem can be decomposed into a set of distinct phenomena, including formation and accumulation of radiation defects, activation of dislocation sources and motion of the dislocations in a high-density environment of obstacles. This sequence can be studied theoretically within a multiscale approach, where different analytical and simulation techniques are applied to particular phenomena and individually validated against specifically designed experiments.

Considerable success has already been achieved in the multiscale modelling of radiation effects in fcc metals. Thus, the primary damage resulting from displacement cascades has been studied by molecular dynamics (MD), revealing the general features of the formation of SFTs and clusters of self-interstitial atoms (SIAs) [16, 17]. Properties of these clusters, such as their stability, mobility and interactions, were also studied by atomic-scale modelling and elasticity theory [18–22]. Further evolution of the microstructure and accumulation of radiation damage were considered in terms of rate theory [23], using properties and mechanisms revealed from atomistic modelling and continuum theory. By way of contrast, less progress has been achieved in understanding mechanical property changes. Up to now, publications on the continuum modelling of deformation in irradiated Cu [24, 25] were based on dislocation dynamics (DD) simulations, which account for collective effects of a population of SFTs on moving dislocations, and also treat the stress conditions arising from the applied stress and the long-range elastic dislocation–dislocation and dislocation–SFT interactions. However, the local rules employed to model the contact between dislocations and SFTs (systematic removal of the SFTs after contact interaction) have been necessarily approximate, so that only qualitative information can be drawn from such simulations. Knowledge of the individual short-range interactions, which are atomic-scale in nature, can be obtained only by systematic studies based on different, mutually validated, techniques.

Three complementary approaches have been applied: experiments using TEM, continuum theory of dislocations and atomistic computer modelling. The first approach is based on TEM observations, which may be *post mortem* or *in situ*. Experiments in which specimens are deformed *in situ* by TEM can reveal important details of the interaction [11, 15, 26, 27], but their spatial and time resolutions ($\sim$10 nm and one image per 1/30 s) restrict observation to relatively large defects (10–50 nm) and low strain rates ($<10^{-2}\,s^{-1}$). Also, the stress state in the foil and effects of free surfaces and image forces are difficult to evaluate because the exact thickness of the TEM samples is not known and varies spatially.

The second approach, continuum elasticity theory, describes large SFTs as a set of stair-rod dislocations and stacking faults (SFs) and can be applied with an accuracy limited to the details of dislocation–dislocation interactions considered at a continuum level [21, 22] or revealed from general properties of dislocations [28]. Small SFTs are beyond the scope of this second approach.

Finally, atomic-scale simulations can be used in principle to investigate all aspects of dislocation–obstacle interactions. As a result of recent developments in atomic-scale dislocation dynamics, considerable success has been achieved in understanding dislocation–obstacle interactions in relation to radiation-induced defects. In particular, interaction of screw and edge dislocations with small glissile [29, 30] and sessile [31, 32] interstitial loops in fcc Ni and bcc Fe [33, 34] has been studied. Interactions with voids and precipitates in bcc Fe and fcc Cu [35, 36] have also been considered. The main restriction in such modelling is that the duration of the simulations is limited to a few nanoseconds, with correspondingly high strain rates ($\sim 10^6$–$10^8\,s^{-1}$). However, this modelling technique corresponds well to the specific conditions of plastic instability and creation of cleared channels in irradiated fcc metals, namely a high number density, up to $\sim 10^{24}\,m^{-3}$, of SFTs with size up to about 6 nm and dislocations moving under a relatively high stress ($\sim$200–300 MPa). To date, no systematic study of dislocation–SFT interactions has been performed. The few studies [37–41] published on dislocation–SFT interactions report mechanisms, such as partial absorption by edge dislocations, and SFT shear and splitting into smaller clusters by both edge and screw dislocations, but the effects of the geometry, temperature and dislocation velocity were not clarified and, therefore, the general picture is still obscure.

In this article, referred to hereafter as Part I, and another following, Part II, we present results of a systematic study at the atomic scale of the interactions between moving edge and screw dislocations and SFTs. In Part I, we report dislocation–SFT interaction mechanisms and demonstrate their dependence on interaction geometry, and investigate effects of temperature, applied strain rate and interatomic potential. The main aim has been to understand the mechanisms of dislocation–SFT interaction at the atomic scale and, more precisely, how SFTs may disappear to leave cleared channels. We demonstrate that complete unfaulting of SFTs never occurs and that the simple shear of the defects is more frequent than generally supposed. We consider here only small SFTs, side length $\leq$4 nm, compatible with *post mortem* TEM observation. The case of larger SFTs and comparison with *in situ* observations will be described elsewhere [42]. The strengthening due to the particular mechanisms and effects of external parameters will be reported in Part II.

2. Computational model

Interactions between moving edge and screw dislocations and a row of SFTs have been studied using the models developed in [31, 43] for either static ($T = 0$ K) or dynamic ($T > 0$ K) conditions. The former approach allows the equilibrium state of a system at a given strain to be determined and the results can be compared directly with those from continuum theory, e.g. equilibrium dislocation shape under a particular applied stress and Burgers vector reactions. The second approach allows temperature and strain rate effects to be studied.

Screw and edge dislocations with Burgers vector $\boldsymbol{b} = 1/2[\bar{1}10]$, gliding in a (111) plane of a fcc crystal containing up to 6.4 million mobile atoms are considered. Figure 1 shows the simulation cell used for a screw dislocation (denoted SD) with axes $x = [\bar{1}10]$, $y = [11\bar{2}]$ and $z = [\bar{1}\bar{1}\bar{1}]$. For a crystal of 6.4 million atoms, dimensions are $L_b \approx 73$ nm, $L \approx 44$ nm and $H = 20$ nm. For this size, most of the crystal potential

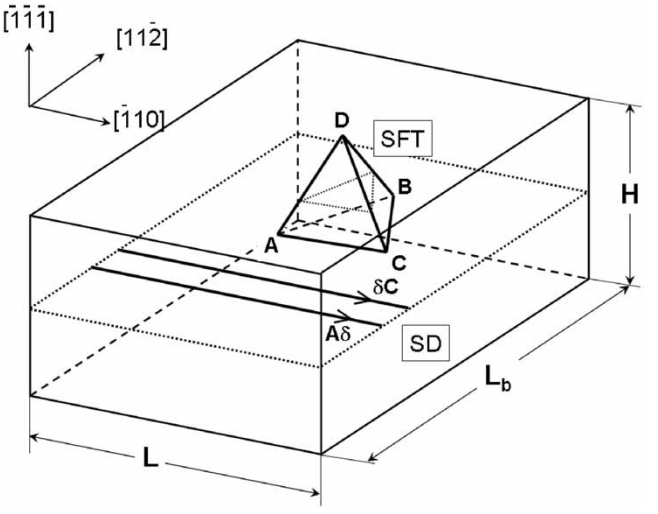

Figure 1. Schematic view of the simulation cell with the corresponding crystallographic orientation. A specific configuration is shown, denoted 'SD/Face' in the text.

energy associated with dislocations is 'elastic', so that enough of the elastic field is included for the atomistic dislocation simulations to compare accurately with dislocation dynamics or quasi-continuum models that assume dislocations to be in infinite elastic media [44, 45]. The dislocation–SFT interaction effects found in the MD simulations below are driven by changes in both the elastic and core energy of the defects, but there does not seem to be any reasonable way of separating them. The details of construction of edge and screw dislocations are described in [29, 43] and [31] respectively.

Periodic boundary conditions are applied along x and y. Two types of boundary conditions were employed in the z-direction. The atoms in slabs within a distance from the upper and lower z surfaces equal to the interatomic potential cut-off radius were either forced to move only in the x and y directions, with no z out-of-plane displacement allowed (two dimensional dynamics: 2-DD) [29–31], or were forced to move rigidly with respect to each other (rigid boundary conditions: RBC) [43]. These two types of boundary condition correspond to two ways of inducing dislocation glide. One is *stress-rate controlled*, which is considered in the case of 2-DD by adding forces of opposite sign to the atoms in the upper and lower slabs. The other is *strain-rate controlled*, which is realized in the case of RBC by displacing the rigid slabs at a constant velocity. Note that RBC can also be used in stress-rate controlled mode [43]. The stress rate was varied from 1 to 10 MPa ps^{-1}, whereas the microscopic strain rate was varied from 5 to 100×10^6 s^{-1}. Stress-rate conditions were used instead of the more classical constant-stress conditions because, in the latter case, the applied stress is either below the critical unpinning stress and no reaction occurs, or is above and the resulting strain rate is high and may be too large to allow the complex reactions described below to proceed, the latter being very sensitive to the strain rate as emphasized in section 5. As will be detailed in Part II, we checked that with both types of boundary condition, the same critical unpinning stresses are obtained for dislocation release from SFT, which indicates that the results presented here do not depend on the boundary conditions. More details on the loading techniques in

atomic-scale dislocation dynamics can be found in [43]. Also, by using the lowest rates compatible with the simulations, we tried to minimize inertial effects.

We used four different embedded atom method (EAM) potentials. Three of them model Cu crystals and mainly differ through their stacking fault energy (SFE). They were developed by Ackland *et al.* [46] (SFE = 20 mJ m^{-2} [32]), Mishin *et al.* [47] (44.4 mJ m^{-2}) and Foiles *et al.* [48] (11.4 mJ m^{-2} [37]). To investigate the influence of other material properties, we also employed a Ni potential, developed by Angelo *et al.* [49], with a higher SFE of 89 mJ m^{-2}.

To assist with understanding the mechanisms involved, special attention was paid to the visualisation of the dislocations and the SFTs throughout the interaction processes. Atoms in defect configurations were visualized using a geometrical method, where the local environment of all atoms in the computational cell is compared to a perfect fcc environment and only those atoms which do not have 12 first neighbours close to fcc positions are shown [31] with a colour that depends on the number of fcc first neighbours found. This method readily identifies dislocation core atoms (dark symbols in later figures) and atoms in intrinsic and extrinsic stacking faults (light symbols).

3. Defect geometries and simulation parameters

Owing to the symmetries of the dislocation geometries, dislocations and SFTs can take only four different configurations with respect to each other, as shown schematically in figures 2 and 3. The edge dislocation (ED) is placed and oriented such that its glide plane, which passes through the bottom of its extra half-plane in figure 2, is the central (111) plane of the simulation cell. The resulting dislocation line and Burgers vector are shown in figure 2. The SFT can take only two orientations with respect to this dislocation, with its apex pointing either up (figure 2a) or down relative to the dislocation glide plane (figure 2b). Note that the grey block arrow in these figures indicates the glide direction of the dislocation. In the following, these configurations will be referred to as 'ED/Up' and 'ED/Down', respectively. (The Greek/Roman letters δA, Cδ in these figures are Burgers vectors in the Thompson tetrahedron notation used later.)

The convention chosen for the screw dislocation (SD) is shown in figure 3. The SFT can take two geometries, with the screw dislocation being on the side of either a face (figure 3a) or an edge (figure 3b) of the SFT. These configurations will be denoted 'SD/Face' and 'SD/Edge', respectively. Kimura and Maddin [28] considered the 'SD/Face' configuration for their unfaulting mechanism.

The other geometrical parameter is n, the number of (111) atomic planes between the SFT base and the dislocation glide plane. In the following, we will denote the height of the SFT in the [111] direction by the number, N, of (111) atomic planes, i.e. the height is $Na_o/\sqrt{3}$, where a_o is fcc lattice parameter. With this notation, the number of vacancies in a perfect SFT is $N_v = N(N+1)/2$; the length of a SFT edge (referred to as the SFT size) is Nb, where b is the magnitude of the perfect dislocation Burgers vector ($a_o/\sqrt{2}$).

We considered SFTs containing from 28 to 136 vacancies, which corresponds to N from 7 to 16 and edge length from ~1.75 to ~4.1 nm. The simulations, therefore, cover the range of SFT sizes observed in irradiated Cu [3].

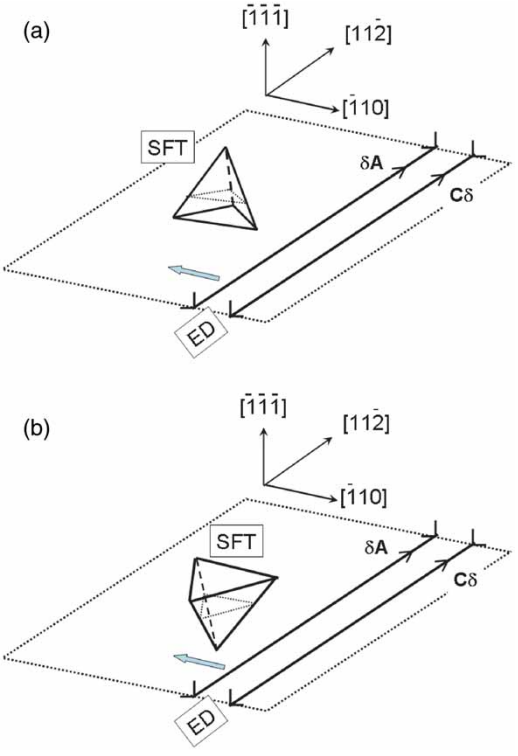

Figure 2. Schematic representation of the two possible configurations involving an edge dislocation: ED/Up (a) and ED/Down (b).

The simulation procedure is as follows. The dislocation is first created in the simulation cell and the atomic configuration is relaxed. The SFT is then introduced in the vicinity of the dislocation by removing atoms in a triangular platelet in a horizontal (111) plane at a number of planes n away from the dislocation glide plane, forming a vacancy-type triangular Frank loop. This new configuration is then relaxed, which allows the Frank loop to dissociate and transform into a perfect SFT, following the classic Silcox–Hirsch mechanism described in [6] and observed in MD [18, 19] and static [20] simulations. We simulated dislocations of length, L, ranging from ~20 to 76 nm, which correspond to the separation between one SFT and its periodic images. This compares with the mean distance between SFTs observed in [3] of about 20 nm.

We have identified six features or parameters that fully characterize a simulation. They have been introduced above and are: (1) the *interatomic potential*, which defines the properties of the material and, in particular, whether the material considered is Cu or Ni; (2) the *dislocation–SFT configuration*, i.e. ED/Up, ED/Down, SD/Face or SD/Edge; (3) the height (or size) N of the SFT; (4) the relative height, n/N, at which the dislocation glide plane intersects the SFT; (5) the *temperature* (equal to zero in the case of static simulations); (6) the *applied stress-* or *strain-rate*.

In the following, a simulation is characterized by specifying the corresponding set of parameters. For example: *Cu Mishin*, *SD/Face*, 11/16, 100 K, 2.5 MPa ps^{-1} is a simulation of a screw dislocation approaching the face of a SFT of 136 vacancies

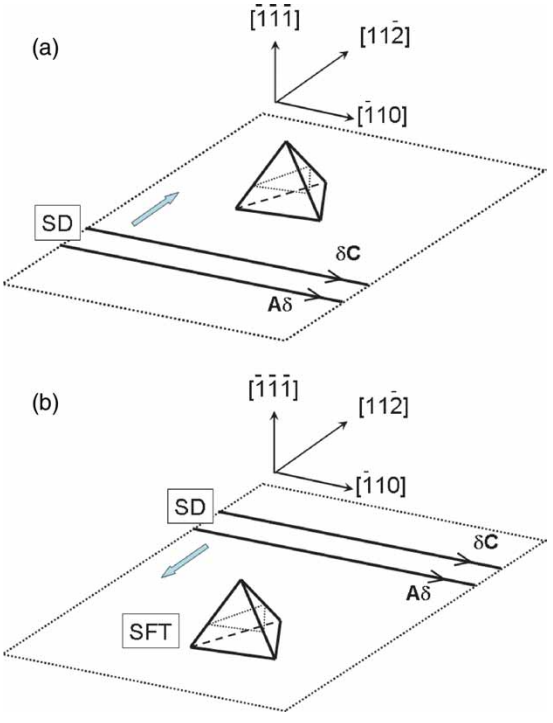

Figure 3. Schematic representation of the two possible configurations involving a screw dislocation: SD/Face (a) and SD/Edge (b).

($N = 16$) at $n = 11$ (111) planes from the base: the crystal is Cu described by the potential of Mishin *et al*. [47] at a temperature of 100 K with an applied stress rate of $\dot{\sigma} = 2.5$ MPa ps^{-1}. When strain-rate-controlled loading is used, the value of $\dot{\varepsilon}$, e.g. $2 \times 10^7\,\mathrm{s}^{-1}$, is indicated instead of the stress rate. We observed several distinct dislocation–SFT interaction mechanisms, depending on the particular set of simulation parameters. Their description and a discussion of parameters that control their probability are presented in the next sections.

4. Results

By systematically varying the simulation parameters introduced above, we observed five qualitatively different outcomes for dislocation–SFT interaction. They are illustrated in this section with specific examples. The parameters that control their occurrence are discussed in section 5. The first reaction, denoted by R1, occurs when both the SFT and the dislocation remain *unchanged* after the interaction. The second reaction (R2) leads to a permanent *shear* of the SFT. The third (R3) corresponds to *absorption* in the dislocation core, which is possible only with edge dislocations that climb with the formation of superjogs. The fourth reaction (R4) is a *partial and temporary absorption* of the SFT by a screw dislocation, which leads to the decomposition of the initial SFT into a set of smaller and weaker obstacles.

Finally, reaction R5 occurs when the dislocation glide plane coincides with the bottom face of the SFT ($n = 0$).

4.1. *Reaction R1: shear followed by complete restoration*

We illustrate this mechanism by a simulation with parameters (*Cu Mishin*, *SD*/*Face*, 11/16, 100 K, 2.5 MPa ps^{-1}). Figure 4 shows defect configurations at different times during the interaction. The Burgers vector geometry is shown in the inset of figure 4a. We use the notation of the Thompson tetrahedron with our choice for the labelling noted on the SFT vertices in the inset of figure 4a. In figure 4a, the δC Shockley partial of the screw dislocation comes into contact with the face of the SFT, soon followed by the second Aδ partial (figure 4b). The dislocation constricts in the face of the SFT but, by way of contrast with other reactions presented below, does not cross-slip in the SFT face. It enters the SFT and shears it (figure 4c). The dislocation then leaves the SFT, with no residual damage on either, as can be seen in figure 4d.

This reaction is also observed in the case of edge dislocations for both the 'ED/Up' and 'ED/Down' configurations. An example for the case (*Cu Ackland, ED*/*Down*, 6/12,100 K, 2×10^7 s^{-1}) is presented in figure 5, where the atoms in the stacking faults have been removed for the sake of clarity. In this case, the δA partial comes into contact with the SFT face (figure 5a) before the second Cδ partial

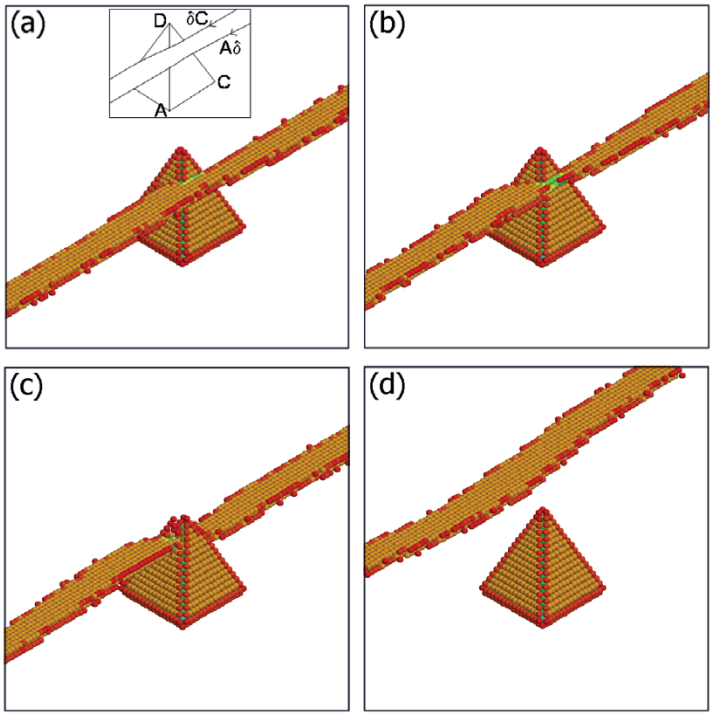

Figure 4. Reaction R1: shear of a SFT by a screw dislocation, followed by full restoration. The simulation parameters are (*Cu Mishin*, *SD*/*Face*, 11/16, 100 K, 2.5 MPa ps^{-1}).

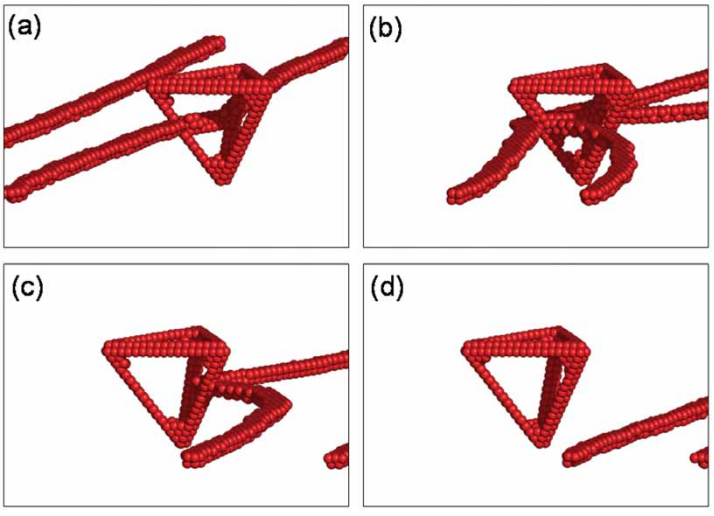

Figure 5. Reaction R1: shear of a SFT by an edge dislocation, followed by full restoration. The simulation parameters are (*Cu Ackland*, *ED*/*Down*, 6/12, 100 K, $2 \times 10^7\,s^{-1}$).

joins in (figure 5b). The partials do not react with the SFT but shear the latter (figure 5c) that is left without being damaged (figure 5d).

With this interaction mechanism, the SFT is sheared by the gliding dislocation and ledges are formed on two faces. These ledges are mobile in the faces, however, and reach the face edges and disappear. The SFT is, therefore, restored in its initial perfect configuration. This reaction is, thus, characterized by an absence of damage on both defects. It is observed with all four possible geometries. As will be emphasized in section 5, the critical criterion for this is that the dislocation must intersect the SFT close to its apex, i.e. with $n/N > 0.5$. Also, low temperature and high strain rate increase the probability of this mechanism.

4.2. *Reaction R2: shear with persistent damage*

Reaction R2 results in residual damage of the SFT with no change imposed on the dislocation. We illustrate this reaction in figure 6 by a simulation with parameters (*Cu Ackland*, *ED*/*Down*, 6/12, 300 K, $2 \times 10^7\,s^{-1}$), i.e. the same simulation as that in the previous section, but with a higher temperature. Again, atoms in the stacking faults are omitted for the sake of clarity.

The SFT is again sheared by the gliding dislocation by a mechanism that will be detailed in the next section, but, by way of contrast with R1, the two ledges formed on the SFT faces are stable. Figure 7a shows an example of the resulting stable ledge configuration on the SFT. Another type of damage is also often observed, resulting in the displacement of generally one or a few vacancies from an apex to an edge of the SFT. An example of such a structure is shown in figure 7b.

When a SFT with stable ledges is sheared by multiple dislocations, two cases have been observed: the damage either accumulates and the SFT is progressively sheared, or after the second passage of a dislocation, the ledges become unstable and the SFT is restored to its initial perfect configuration. The latter reaction is believed

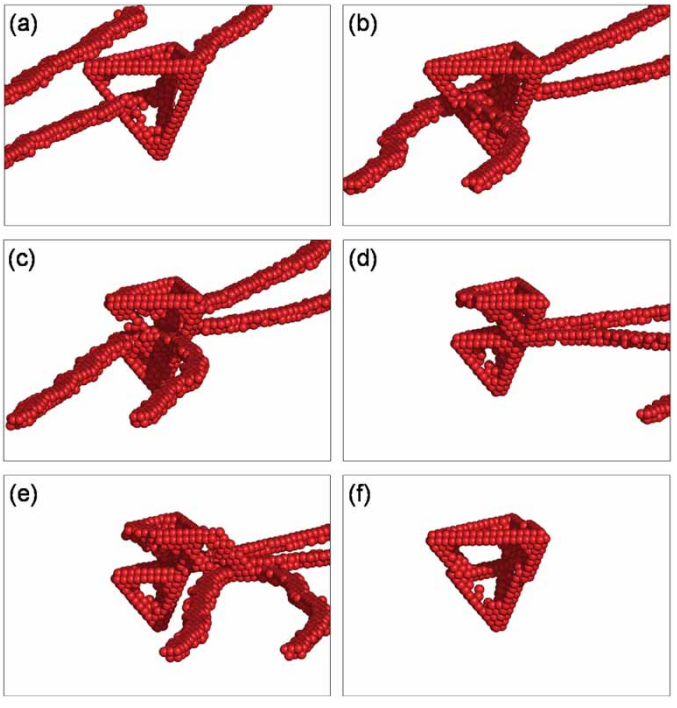

Figure 6. Reaction R2: shear of a SFT by an edge dislocation. The simulation parameters are (*Cu Ackland*, *ED*/*Down*, 6/12, 300 K, $2 \times 10^7\,s^{-1}$).

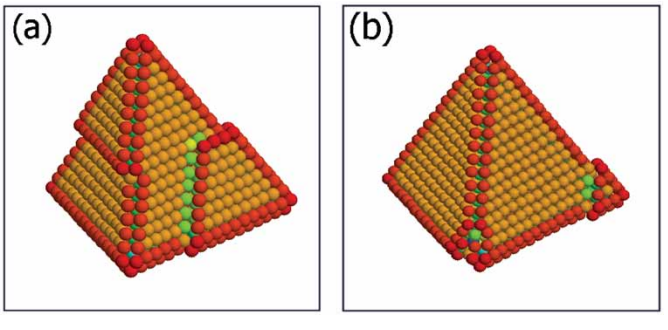

Figure 7. Example of (a) stable ledge configuration and (b) a vacancy transported from one apex to another. The simulation parameters are (a) (*Cu Mishin*, *ED*/*Down*, 3/16, 100 K, 2.5 MPa ps^{-1}) and (b) (*Cu Mishin*, *ED*/*Down*, 7/16, 100 K, 2.5 MPa ps^{-1}), respectively.

to arise because the ledges of height equal to 2b have high energy: they become mobile and annihilate on the borders of the SFT faces, as in reaction R1.

4.3. *Reaction R3: partial absorption into edge dislocations*

This mechanism concerns only edge dislocations in the 'ED/Down' configuration, i.e. when the extra-half plane of the dislocation is oriented towards the base of

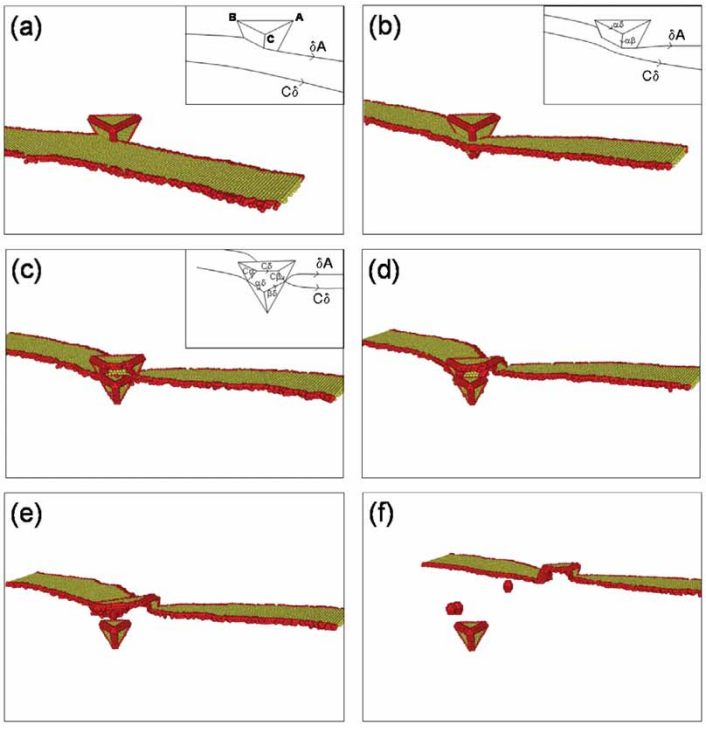

Figure 8. Reaction R3: partial absorption into an edge dislocation. The simulation parameters are (*Cu Ackland*, *ED*/*Down*, 6/12, 300 K, $2 \times 10^7\,s^{-1}$).

the SFT. This reaction is favoured by high temperature, small n/N value and large SFT size: the 3.2 nm SFT ($N = 12$) is the smallest for which this reaction was observed. We illustrate it in figure 8 with the simulation (*Cu Ackland*, *ED*/*Down*, 6/12, 450 K, $2 \times 10^7\,s^{-1}$). In figure 8a, the δA Shockley partial of the edge dislocation comes into contact with the face of the SFT, soon followed by the Cδ partial (figure 8b). The δA partial slips through the SFT, while the Cδ partial reacts with the $\alpha\beta$ stair-rod partial edge of the SFT (figure 8c). The Burgers vectors taking part in the reaction are shown in the insets. In figure 8d, the CA dislocation detaches from the SFT on the right-hand side, with the formation of a jogged segment, which is clearly visible in the figure. Note that the height of the latter is exactly n. The CA dislocation then detaches completely from the SFT (figure 8e).

The net result of this reaction is the absorption in the dislocation of the part of the SFT between its base and the glide plane, which causes the dislocation to climb with the formation of a pair of superjogs along its line. The jogs inherit the initial shape of the SFT, with the consequence that one jog lies in a {111} plane and is glissile, while the other jog is in a {100} plane and is a constricted segment of a Lomer dislocation. This dislocation is well-known to have a low mobility. Further motion of the jogged dislocation creates small vacancy clusters, which are visible in figure 8f. The corresponding interstitials are absorbed in the sessile jog to enable it to change shape and plane and become glissile. A similar reaction was observed in the case of superjogs created after absorption of an interstitial cluster [29].

4.4. *Reaction R4: partial and temporary absorption into screw dislocations*

Reaction R4 concerns only screw dislocations in the 'SD/Face' configuration, i.e. when the dislocation comes into contact with one face of the SFT. This configuration was considered by Kimura and Maddin [28], who proposed a mechanism based on the cross-slip of the screw dislocation in the SFT face that could lead to complete absorption of the SFT by formation of a helical turn on the screw dislocation. As will be shown below, only partial absorption was observed in the present simulations.

The reaction is illustrated in figure 9 by a simulation with parameters (*Cu Mishin*, *SD/Face*, 7/16, 100 K, 2.5 MPa ps^{-1}). In figure 9a, the δC partial of the screw dislocation comes into contact with the face of the SFT. Spontaneously, the second partial also comes into contact with this face and the dislocation constricts. It then cross-slips and dissociates in the SFT face into two partials, βC and βA. As seen in figure 9b, the βA partial sweeps over the part of the SFT face below the glide plane and removes the stacking fault in this region. The βC partial remains immobile. When the βA partial combines on the right-hand side of the SFT with the $\beta\alpha$ stair-rod, it forms a Frank partial with an Aα Burgers vector. This high-energy partial is unstable and dissociates into dislocations with Burgers vectors AC and Cα.

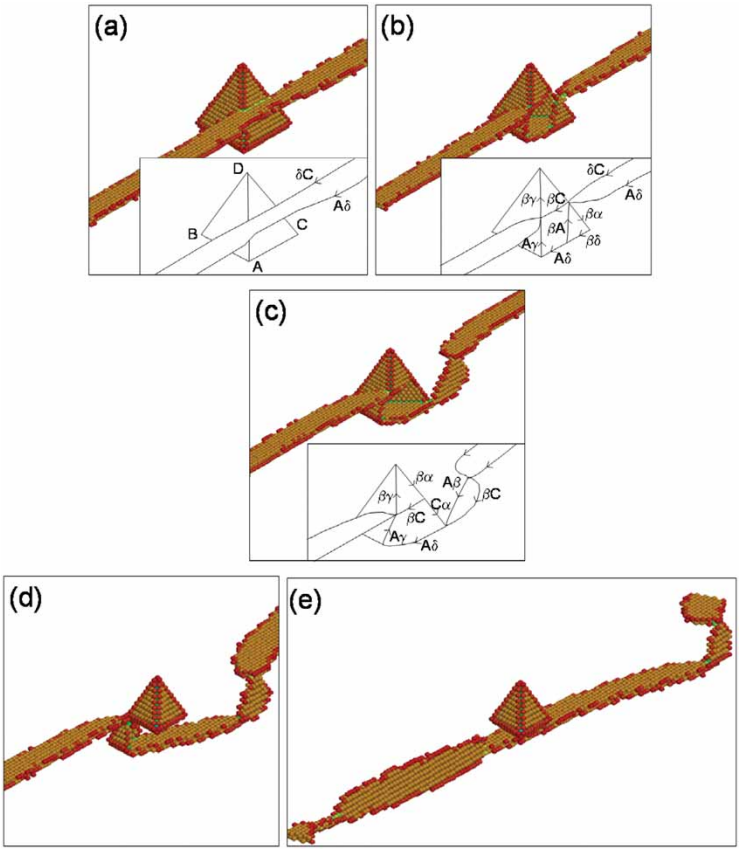

Figure 9. Reaction R4: partial absorption into a screw dislocation. The simulation parameters are (*Cu Mishin*, *SD/Face*, 7/16, 100 K, 2.5 MPa ps^{-1}).

The AC segment is a cross-slipped segment of the initial screw dislocation. It dissociates with the formation of a constricted node, as can be seen on the right-hand-side of the SFT in figure 9c. This cross-slipped segment moves away from the SFT, as seen in figure 9d. On the other side of the SFT, the screw dislocation starts to cut the SFT, forming a new stacking fault on the cut plane and, thereby, effectively recreating a smaller tetrahedron. When it reaches the edge (figure 9e), it also leaves the SFT. The net result, shown in figure 9e, is that a helical turn was formed on the screw dislocation and is dissociated in several {111} planes and the SFT now has a reduced size, but has not been completely absorbed by the screw dislocation.

The reaction mechanism observed here is different from that proposed by Kimura and Maddin [28] in two respects. Firstly, these authors supposed that both the βC and βA cross-slipped partials would sweep the SFT face and fully remove the fault of this face, while in reality only one partial is mobile and unfaults only the bottom part of the SFT. They also assumed that the Aα Frank partial would remain constricted, whereas it decomposes and forms a cross-slipped segment for the screw dislocation that leaves the SFT and forms the helical turn.

Reaction R4 is the equivalent of reaction R3 for edge dislocations. The result for the SFT is the same, i.e. absorption of the portion between its base and the dislocation glide plane. However, by way of contrast with the edge case, the screw dislocation cannot drag the vacancies by its motion and has to unpin from the helical turn before gliding further. The helical turn can only glide in the direction of its Burgers vector and not in the glide direction of the screw dislocation. The unpinning mechanism (studied in detail in [31]) requires the dislocation to bow out and force the SFT to close onto itself. When the dislocation unpins, the vacancies that were in the helical turn are left in the form of a vacancy cluster aligned in a ⟨110⟩ direction. The cluster is displaced from the initial SFT in the ⟨110⟩ direction of the screw Burgers vector. The number of vacancies in this cluster is equal to the difference between the number N_V in the original and in the new tetrahedra, and so depends on n. The distance between the resulting parts depends on the ability of the helical turn to glide along the dislocation line and, therefore, depends on the curvature of the dislocation, which in turn depends on the stress/strain rate. An example of this process is presented in figure 10 with simulations for (*Cu Ackland*, *SD*/*Face*, 6/12, 300 K) at different strain rates. Figure 10b presents the result of the interaction at strain rate $\dot{\varepsilon}=10^7\,\mathrm{s}^{-1}$, whereas the result of the same simulation at $\dot{\varepsilon}=5\times10^7\,\mathrm{s}^{-1}$ is presented in figure 10c. The distance between the residue of the original tetrahedron and the newly created vacancy cluster is significantly larger for the lower value of $\dot{\varepsilon}$, i.e. ~25 *versus* ~4 nm, respectively. The structure of the new vacancy cluster is rather complicated and consists of two large stacking faults parallel to the base of the original SFT. In this series of simulations, the practical value of the lower strain rate was limited by the size, L, of the simulated crystal along the dislocation line.

4.5. *R5: dislocation glide plane and SFT base plane coincide*

We observed reactions that cannot be attributed to the four categories described above. These occurred for the situation when, at finite temperature, either the screw or edge dislocation slip plane is close to or coincident with the SFT base plane. The vacancies from the base plane may then be taken away from the SFT. This is illustrated in figure 11 for the case (*Cu Ackland*, *SD*/*Face*, 1/16, 300 K, $10^7\,\mathrm{s}^{-1}$).

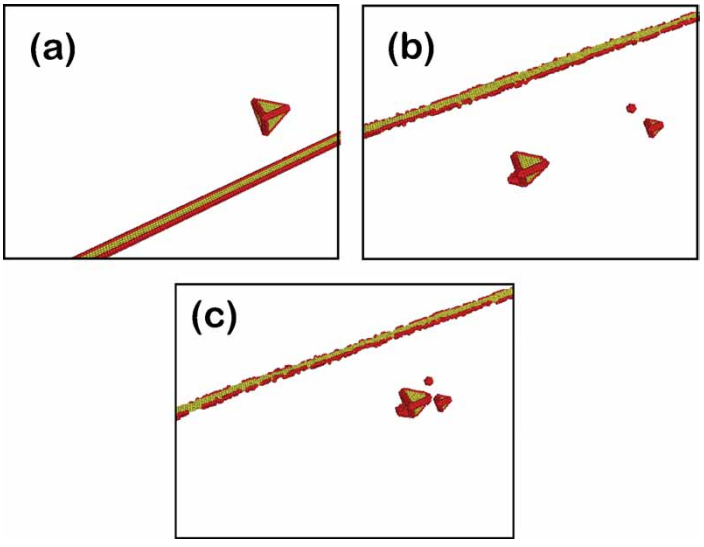

Figure 10. Examples of structural changes after reaction R4 (*Cu Ackland*, *SD/Face*, 6/12, 300 K): (a) initial configuration and after deformation at (b) $\dot{\varepsilon} = 2 \times 10^7\,s^{-1}$ and (c) $\dot{\varepsilon} = 5 \times 10^7\,s^{-1}$.

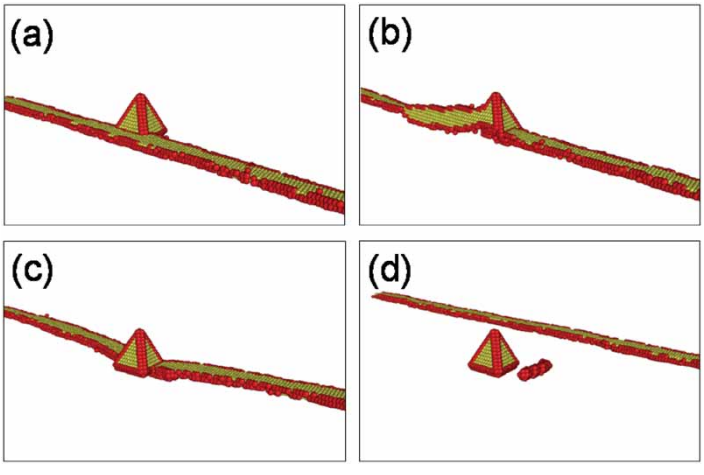

Figure 11. Case of a screw dislocation that impinges on the bottom plane of a SFT (*Cu Ackland*, *SD/Face*, 1/12, 300 K, $5 \times 10^6\,s^{-1}$), with the vacancies on this plane removed and left as a row near the SFT. Note that vacancies are displaced not only along the screw dislocation line but also along the dislocation glide direction.

As in figure 9, the screw dislocation comes into contact with the SFT face (figure 11a) and cross-slips (figure 11b). However, due to a line tension effect produced by the curvature of the dislocation, the constricted node on the left side of the SFT comes back and the dislocation sweeps the lower plane of the SFT (figure 11c). When the dislocation unpins, the vacancies that were in the lower plane are removed and form a cluster clearly visible in figure 11d. Interestingly, unlike the

R4 mechanism when the new vacancy cluster is separated from the SFT base along the direction of the dislocation Burgers vector (see figure 10), vacancies in this case are also displaced along the dislocation motion direction, as can be seen in figure 11. This is the only mechanism for which we observed vacancy transport along the screw dislocation glide direction. It is rather insensitive to strain/stress rate, for we have observed exactly the same result within the strain rate range from 5×10^6 to $10^8\,s^{-1}$.

5. Discussion

The five interaction mechanisms identified here were observed with all interatomic potentials and so do not depend on either the potential or the material (Cu or Ni). In particular, they do not depend on the dissociation width of the dislocations, for they are observed in models of both the Ackland *et al*. [46] potential (low stacking fault energy $\sim 20\,mJ\,m^{-2}$) and the Mishin *et al*. [47] potential (higher stacking fault energy $44.4\,mJ\,m^{-2}$). As will be emphasized below, some of these reactions were also observed by other authors who employed different potentials and methods. However, quantitative results, such as critical size and critical strain/stress rate, depend on the potentials. Also, the comparison between 2-DD/stress-rate controlled simulations and RBC/strain-rate controlled simulations shows that the results obtained here do not depend on the boundary conditions used.

The main parameter that controls the probability of occurrence of the different reactions is the dislocation/SFT geometry, since the two reactions R3 and R4 occur only for the specific configurations 'ED/Down' and 'SD/Face', respectively, while the other reactions are observed with all configurations. The other parameters that affect the probability are the relative height of the dislocation glide plane (n/N), the temperature and the stress/strain rate. Reaction R1 is the most frequent but does not lead to residual damage on either the dislocation or the SFT. It, therefore, plays no part in clear band formation but does contribute to hardening (see Part II). The probability of this reaction increases with decreasing temperature or increasing stress/strain rate and it occurs when the dislocation glide plane is close to the SFT apex ($n/N > 0.5$).

Reactions R3 and R4 result in substantial damage to the SFT but are of lower probability than reaction R1. They result in absorption of the bottom part of the SFT into the core of the dislocation. In the edge case (reaction R3), drag of the absorbed part of the defect in the form of a pair of superjogs is possible. In the screw case (reaction R4), the vacancies form a helix turn that cannot be dragged and, after unpinning of the dislocation by the applied stress, the vacancies are left as a cluster in the dislocation Burgers vector direction at a distance away from the initial SFT that depends on the strain/stress rate, as illustrated in figure 10. The probability of reactions R3 and R4 increases with increasing temperature and/or decreasing stress/strain rate and, in general, they occur when the dislocation glide plane is close to the SFT base ($0 < n/N < 0.5$). However, at high temperature and low strain rate, R4 can occur at $n/N > 0.5$. For example, we have observed this reaction for the case (*Cu Ackland*, *SD/Face*, 8/12, 450 K, $5 \times 10^6\,s^{-1}$). This case is also characterized by the largest separation between the displaced cluster and the residual apex part of the SFT ($\sim$45 nm) and the smallest size of the latter ($\sim$1 nm and 10 vacancies).

Also, in the edge case, reaction R3 occurs only with large SFTs with $N \geq 16$. On the other hand, we did not observe any limitation on SFT size in the screw case.

Reaction R2 is intermediate between R1 and R3/R4. It leads to limited change, with the SFT being sheared by at most one Burgers vector. It may play a role in clear band formation, but requires the passage of multiple dislocations. (It is well-known that clear bands are initiated by the passage of a piled-up group of dislocations [15]). If repeatedly intersected by dislocations, this mechanism can lead to the separation of the original SFT into two parts, a smaller SFT in the apex part of the original SFT and an irregular, heavily faulted vacancy cluster in the base part, which has a low stability. Effectively, this '*multiple R2*' reaction is equivalent to reaction R4. Note also that reaction R2 often appears as an aborted R3 or R4 mechanism. Indeed, the reaction shown in figure 6a–e is similar to that in figure 8a–d. The difference is that, in figure 6e, the second jog is not able to form and as a consequence the dislocation unpins and simply shears the SFT, whereas, in figure 8e, f, the jog forms and the dislocation drags away the base part of the SFT.

The main parameter that controls the relative probability of occurrence of R2 with respect to R3/R4 is the time available for the dislocation to react. Decreasing the temperature and/or increasing the strain/stress rate favours reaction R2. With increasing temperature, the reactions tend to evolve from R1 to R2 then R3/R4. This trend is illustrated in figures 5, 6 and 8, which show simulations with the same parameters (*Cu Ackland*, *ED*/*Down*, 6/16, $5 \times 10^6\,s^{-1}$) and increasing temperature (100, 300 and 450 K). The result is a transition from R1 at 100 K, to R2 at 300 K and then R3 at 450 K. The higher the temperature, the larger the damage caused to the SFT. Similarly, with decreasing stress or strain rates, the reactions tend to evolve from R1 to R3/R4, as illustrated in figure 10. This figure presents the final configuration of simulations with same parameters (*Cu Ackland*, *SD*/*Face*, 6/12, 300 K) and decreasing strain rate, and shows that, at low strain rate (2×10^7 and $5 \times 10^7\,s^{-1}$), half of the SFT is absorbed in the dislocation *via* reaction R4, while at the higher strain rate ($1 \times 10^8\,s^{-1}$), the SFT is simply sheared.

Reaction R2 has been reported previously in the literature. Wirth *et al.* [37] considered the 'ED/Up' configuration in a Cu crystal simulated at 100 K and observed that the initial perfect SFT was progressively sheared by the multiple passage of an edge dislocation. Szelestey *et al.* [41] considered 'SD/Face' and 'SD/Edge' configurations in a Ni crystal modelled with two different interatomic potentials. They considered the case $n/N = 0$, when the dislocation glide plane coincides with the bottom plane of the SFT, and observed reaction R5, with the vacancies from the bottom plane being carried away from the SFT during the interaction. For $n/N > 0$, they observed SFT shear with reaction R2. The probable reason why the authors of these studies did not observe reactions R3 and R4 is because they performed constant-stress simulations, resulting in high strain rate and high-velocity dislocations. These conditions favour reactions R1 and R2, as discussed above.

Moving dislocations can remove sessile irradiation defects to form a clear band by three mechanisms: (1) absorption and drag of the defects in the dislocation core, (2) transformation of the defects into a weaker configuration, (3) shear of the defects until they become unstable and/or are absorbed in the dislocation core. In the present case of SFTs, we observed either *partial* absorption (reaction R3) or shear by one (reaction R2) or several (reaction R4) Burgers vectors. Transformation of the whole SFTs is not observed, as opposed to the case of Frank loops [31].

However, shear by reaction R4 leads to a transformation of the base part of initial SFT into a heavily faulted irregular vacancy cluster which is less stable and a weaker obstacle. Also, no simulations resulted in complete absorption of the SFTs: only the lower part of the SFT may be absorbed. The latter observation is consistent with *in situ* TEM experiments [26]

Therefore, we can conclude from the present simulations that mobile dislocations, which glide in a slip band, can progressively decompose SFTs into a set of smaller vacancy clusters, such as smaller SFTs, irregular vacancy clusters and/or even single vacancies, separated by a significant distance. These small SFTs and clusters may become unstable and decompose thermally and, thus, disappear from TEM contrast. We have seen that some vacancies can be displaced from the SFT along either the dislocation Burgers vector direction (reactions R3 and R4) or the glide direction (reaction R3 and special case of R5 for $n = 0$). Vacancies can, thus, reach sinks, such as grain boundaries or surfaces, and disappear. However, such vacancy drag cannot occur over a long range and the majority of the vacancies would still remain within the dislocation slip band. This process should, therefore, give rise to a high concentration of small vacancy clusters left in the clear bands, clusters that are too small to be visible in TEM. The mechanism of clear channels formation suggested here should also operate in any system where one type of defect cluster dominates in the microstructure, i.e. secondary phase precipitates formed in supersaturated alloys after ageing [50].

6. Conclusions

By means of an extensive programme of atomic-scale simulations, we have identified and characterized five possible interaction mechanisms between edge and screw dislocations and SFTs. We observed that both edge and screw dislocations can interact by means of three reactions, two of them are shared by both types of dislocation and one is specific to either edge or screw. We have also found that the most probable scenario for clear band formation is a progressive shear of the SFT by multiple dislocation interactions down to sizes where they become unstable. The shear may be of only one or several Burgers vectors per interaction, depending on the dislocation type and strain/stress rate. All cases of damage to a regular SFT lead to a significant reduction in stability of the original SFT, due to either the formation of ledges or the reduction of SFT size and creation of less stable, irregular, heavily-faulted vacancy clusters or even single vacancies. We note that a screw dislocation is significantly more effective in the destruction of an SFT *via* this reaction (R4) than an edge (R2). For example, we have observed reduction of an SFT from 1.8 nm ($N_V = 28$) to 1 nm ($N_V = 10$) *via* a single interaction with a screw dislocation.

Since no long-range transport of vacancies is expected, we conclude that there should be a high concentration of small vacancy clusters and single vacancies in the clear deformation bands. This conclusion could be checked experimentally, in principle, by annealing treatments on deformed specimens.

The critical shear stress for dislocation unpinning and the corresponding resistance to long-range dislocation motion depends strongly on the type of reaction: reaction R1 being the weakest and reactions R4/R5 the strongest. The type of

reaction and, hence, critical stress also depend strongly on the temperature and strain rate. Details of these aspects are required in a multiscale approach in order to construct local rules to be implemented in continuum dislocation dynamics, and will be the topic of Part II [51].

Acknowledgements

The authors thank Dr R. E. Stoller, Dr S. J. Zinkle, Dr Y. Matsukawa, Dr B. N. Singh and Dr B. D. Wirth for stimulating discussions. This research was sponsored by the Division of Materials Sciences and Engineering and the Office of Fusion Energy Sciences, US Department of Energy, under contract DE-AC05-00OR22725 with UT-Battelle, LLC.

References

[1] S. J. Zinkle, L. E. Seitzman, and W. G. Wolfer, Phil. Mag. A **55** 111 (1987).
[2] B. N. Singh and S. J. Zinkle, J. Nucl. Mater. **206** 212 (1993).
[3] B. N. Singh, D. J. Edwards, and P. Toft, J. Nucl. Mater. **299** 205 (2001).
[4] Z. Yao, R. Schäublin, and M. Victoria, J. Nucl. Mater. **307/311** 374 (2002).
[5] R. Schäublin, Z. Yao, N. Baluc, *et al*., Phil. Mag. **85** 769 (2005).
[6] J. Silcox and P. B. Hirsch, Phil. Mag. **4** 72 (1959).
[7] R. E. Smallman and K. H. Westmacott, Mater. Sci. Eng. **9** 249 (1972).
[8] M. Kiritani, Mater. Chem. Phys. **50** 133 (1997).
[9] M. Kiritani, Mater. Sci. Eng. A **350** 1 (2003).
[10] S. Amelynckx, in *Dislocations in Solids*, edited by F.R.N. Nabarro (North-Holland, Amsterdam, 1979), Vol. 2, p. 67.
[11] Y. Dai and M. Victoria, Acta Metall. **45** 3495 (1997).
[12] M. Niewczas, Phil. Mag. A **82** 393 (2002).
[13] J. V. Sharp, Phil. Mag. **16** 77 (1967).
[14] L. M. Howe, Radiat. Effects **23** 181 (1974).
[15] J. S. Robach, I. M. Robertson, and B. D. Wirth, Phil. Mag. **83** 955 (2003).
[16] Y. N. Osetsky and D. J. Bacon, Nucl. Instrum. Methods B **180** 85 (2001).
[17] D. J. Bacon, Y. N. Osetsky, R. E. Stoller, *et al*., J. Nucl. Mater. **323** 152 (2003).
[18] V. G. Kapinos, Y. N. Osetsky, and P. A. Platonov, J. Nucl. Mater. **165** 286 (1988).
[19] B. D. Wirth, V. V. Bulatov, and T. Diaz de la Rubia, J. Nucl. Mater. **283/287** 773 (2000).
[20] Y. N. Osetsky, A. Serra, M. Victoria, *et al*., Phil. Mag. A **79** 2259 (1999); *ibid* 2285.
[21] M. Hiratani, H. M. Zbib, and B. D. Wirth, Phil. Mag. A **82** 2709 (2002).
[22] M. Hiratani, V. V. Bulatov, and H. M. Zbib, J. Nucl. Mater. **329/333** 1103 (2004).
[23] S.I. Golubov, B.N. Singh, H. Trinkaus, *et al*., Private communication (2005).
[24] T. Diaz de la Rubia, H. M. Zbib, T. A. Khraishi, *et al*., Nature **406** 871 (2000).
[25] N. M. Ghoniem, S. H. Tong, B. N. Singh, *et al*., Phil. Mag. A **81** 2743 (2001).
[26] Y. Matsukawa and S. J. Zinkle, J. Nucl. Mater. **329/333** 919 (2004).
[27] R. Shäublin, Z. Yao, P. Spätig, *et al*., Mater. Sci. Eng. A **400/401** 251 (2005).
[28] H. Kimura and R. Maddin, in *Lattice Defects in Quenched Metals*, edited by R. Cotterill (Academic Press, New York, 1965), pp. 319–386.
[29] Phys. Rev. B **61** 8714 (2000).
[30] D. Rodney, Y. Bréchet, and G. Martin, Mater. Sci. Eng. A **309/310** 198 (2001).
[31] D. Rodney, Acta Mater. **52** 607 (2004).

[32] D. Rodney, Nucl. Instrum. Methods Phys. Res. B **228** 100 (2005).
[33] Y.N. Osetsky, D.J. Bacon, and Z. Rong, Phil. Mag. Lett. **84** 745 (2005).
[34] Z. Rong, Y. N. Osetsky, and D. J. Bacon, Phil. Mag. **85** 1473 (2005).
[35] Y. N. Osetsky, D. J. Bacon, and F. Mohles, Phil. Mag. **83** 3623 (2003).
[36] Y. N. Osetsky and D. J. Bacon, J. Nucl. Mater. **323** 268 (2003).
[37] B. D. Wirth, V. V. Bulatov, and T. Diaz de la Rubia, J. Eng. Mater. Technol. **124** 334 (2002).
[38] Y. N. Osetsky, D. J. Bacon, B. N. Singh, *et al*., J. Nucl. Mater. **307/311** 852 (2002).
[39] Y. N. Osetsky, R. E. Stoller, and Y. Matsukawa, J. Nucl. Mater. **329/333** 1228 (2004).
[40] Y. N. Osetsky, D. Rodney, R. E. Stoller, *et al*., Mater. Sci. Eng. A **400/401** 370 (2005).
[41] P. Szelestey, M. Patriarca, and K. Kaski, Model. Simul. Mater. Sci. Eng. **13** 541 (2005).
[42] Y. N. Osetsky, Y. Matsukawa, R. E. Stoller, *et al*., Phys. Rev. Lett. (2006) submitted.
[43] Y. N. Osetsky and D. J. Bacon, Model. Simul. Mater. Sci. Eng. **11** 427 (2002).
[44] R. Madec, B. Devincre, L. Kubin, *et al*., Science **301** 1879 (2003).
[45] Y. N. Osetsky, S. I. Golubov, and R. E. Stoller, Phil. Mag. Lett. (2006), in preparation.
[46] G. J. Ackland, G. Tichy, V. Vitek, *et al*., Phil. Mag. A **56** 735 (1987).
[47] Y. Mishin, D. Farkas, M. Mehl, *et al*., Phys. Rev. B **63** 224106 (2001).
[48] M. Foiles, M. Baskes, and M. Daw, Phys. Rev. B **33** 7983 (1986).
[49] J. Angelo, N. Moody, and M. Baskes, Model. Simul. Mater. Sci. Eng. **3** 289 (1995).
[50] A. Luft, Prog. Mater. Sci. **35** 97 (1991).
[51] Y.N. Osetsky, D. Rodney, and D.J. Bacon, Phil. Mag. (2005), to be submitted.